




Coherent structures associated with interscale energy transfer in turbulent channel flows

Hongping Wang ^{1,2}, Zixuan Yang^{1,2}, Ting Wu ^{1,2} and Shizhao Wang ^{1,2,*}

¹*The State Key Laboratory of Nonlinear Mechanics, Institute of Mechanics, Chinese Academy of Sciences, Beijing 100190, China*

²*School of Engineering Sciences, University of the Chinese Academy of Sciences, Beijing 100049, China*



(Received 11 May 2021; accepted 21 September 2021; published 7 October 2021)

We analyze the energy spectra, production spectra, and interscale energy transfer spectra for direct numerical simulation data of turbulent channel flows at $Re_\tau = 180$ and 550. The transfer spectra are characterized by a negative region and a positive region. We use the negative region as a spectral mask to separate the flow fields into large-scale and small-scale fields. The former are characterized by streaks and quasi-streamwise vortices, and the latter are characterized by hairpin-like vortical structures that are similar to the original flow fields. Proper orthogonal decomposition and linear stochastic estimation are utilized to further extract the flow structures of the decomposed fields. The outer large-scale low-momentum regions are flanked by large quasi-streamwise vortices that are attached to the wall. This coherent structure presents a high degree of similarity to the structure of the near-wall cycle. This result indicates that the outer large scales may present a self-sustaining mechanism similar to that of the near-wall region. We also extract the coherent structures associated with the real-space energy transfer. The formation of small-scale hairpin-like vortices is related to the large-scale shear layer. Within this process, the energy is transferred from large scales to small scales.

DOI: [10.1103/PhysRevFluids.6.104601](https://doi.org/10.1103/PhysRevFluids.6.104601)

I. INTRODUCTION

Wall-bounded turbulent flow is a multiscale and nonlinear dynamic system and is of great importance to engineering applications. On the one hand, coherent structures, such as near-wall streaks, hairpin vortices, large-scale motions (LSMs), and very-large-scale motions (VLSMs), hierarchically distribute over different wall-normal locations and present a broad range of time-space scales [1–8]. On the other hand, the energy cascade is also a multiscale property of turbulence [9]. The kinetic energy enters the turbulence through the production mechanism at the largest scales of motion and is then transferred to successively smaller scales until the energy is dissipated by viscous action [10,11]. Energy transfer and redistribution have been investigated in many studies [12–20]. However, there have been only a limited number of studies the goal of which is to find the relationship between energy transfer and coherent structures. The flow structures related to the energy transfer are expected to provide some insights into the self-sustaining process in real turbulent flows.

The turbulent kinetic energy (TKE) budget, including production, transport, and dissipation, has been studied in physical space [10]. It is also meaningful to examine the energy transfer in the scale space to obtain a better understanding of turbulence [21]. As early as 1964, Lumley [22] calculated the budget equation of the energy spectra through the Fourier transform of the two-point correlation

*wangsz@lnm.imech.ac.cn

function of the velocity fluctuations in wall turbulence. Lumley provided the forms and physical interpretations of the various terms. Turbulent energy transport contains interscale transport and spatial transport [14,17,23]. The former is related to the energy transfer in the space of scales, which is consistent with the classical Kolmogorov cascade [9] and results in a broad and continuous energy spectrum [17]. The latter is determined by the spatial redistribution of energy due to the inhomogeneity. The focus of the present paper is on interscale transfer. Domaradzki *et al.* [24] used the results of direct numerical simulation (DNS) to investigate the nonlinear transport of the TKE, especially the interscale transfer. They found that the energy is directly received from the mean flow by the largest eddies and is subsequently transferred to smaller scales by nonlinear interactions. The spectral energy transfer process and the scale interactions in a turbulent channel flow have been investigated using the one-dimensional spanwise spectra of the TKE budget equation [18]. Those authors analyzed the turbulence production and pressure-strain spectra to reveal that the self-sustaining process is presumably the dominant dynamic of the energy-containing motions. Lee and Moser [25] used the DNS data of incompressible turbulent channel flow to investigate the terms in the Reynolds stress transport equations at friction Reynolds number Re_τ up to 5200. The detailed spectral analysis provides much more detail about the energy flow. Recently, Symon *et al.* [26] found that the energy transfer is nearly zero for the optimal (first) resolvent mode, and they proposed using the eddy viscosity to model the nonlinear transfer for each scale.

Coherent structures are another important topic of wall-bounded turbulence [27]. Generally, hairpin-like vortices have been identified as the dominant coherent flow structures in wall turbulence [1,28–31]. In the buffer layer, the legs of hairpin vortices are quasi-streamwise vortices that induce low-momentum fluid upwards, which forms near-wall low-speed streaks [2]. The streaks and streamwise vortices form a self-sustaining cycle and maintain independence of the outer-layer turbulence [32–34]. Although the near-wall cycle can be regarded as universal [35,36], it is still superposed and modulated by the outer large scales [37–39]. The generation of hairpin vortices and wave packets in an artificially triggered turbulent spot was numerically studied by Brinkerhoff and Yaras [30]. The instability of the shear layer in the streamwise-spanwise plane induced by the legs of hairpin vortices is a critical mechanism for the formation of hairpin vortices along the spanwise edges of the spot. In the inner layer of the fully developed turbulent boundary layer, turbulent-turbulent spots, which are the dense concentration of small-scale vortices with high swirling strength, are also observed by Wu *et al.* [40]. These turbulent-turbulent spots are promising candidates to act as fundamental building blocks of wall-bounded turbulence. The streamwise alignment of a group of hairpin vortices can form LSMs the streamwise length scale of which is approximately $2-3\delta$ [2,3], where δ is the boundary layer thickness. The streamwise length scale of VLSMs is approximately 10δ . However, there has been no scientific consensus about the origin of the outer large scales [3]. Sharma and McKeon [41] suggested that energetic streamwise structures arise naturally from resolvent analysis rather than by a summation of hairpin packets. Rawat *et al.* [42] computed the invariant solutions for large-scale structures using an overdamped large-eddy simulation and found that the energy-containing motions are self-sustaining. The outer energy-containing motions are also composed of streamwise-elongated streaks and short vortical structures [8,43].

It is significant to investigate the relationship between energy transfer and coherent structures. The near-wall cycle consists of three sequential subprocesses: streak formation, streak breakdown, and vortex regeneration [32,44]. The formation of streaks is created by the convection of streamwise vortices, and the breakdown is ascribed to the instability of the streak structures, which can generate three-dimensional velocity fluctuations. The nonlinear interactions of the three-dimensional velocity fluctuations reenergize the streamwise vortices. According to Hamba [21], this cycle is related to the energy transfer. Streak formation and streak breakdown correspond to a forward energy cascade, whereas vortex regeneration corresponds to a backward energy cascade. Recent studies have also found that the logarithmic layer has a self-sustaining motion similar to that of the buffer layer [45–47]. Kawata and Alfredsson [48] analyzed the scale-by-scale transport of the Reynolds shear stress. They revealed that the small scales near the wall indeed influence the large-scale structure

in the channel core region. This inverse interscale transport of Reynolds shear stress ultimately supports the production of turbulent energy at large scales. However, their studies are limited to low Reynolds numbers. A three-dimensional flow structure of the kinetic energy transfer in shear turbulence is given by Dong *et al.* [49], which contains an upright hairpin and an inverted hairpin. Wang *et al.* [20] revealed the structural characteristics associated with energy transfer using particle image velocimetry fields at low-to-moderate Reynolds numbers. The large scales are extracted using the zero-crossing scale boundary in the two-dimensional energy transfer spectrum, and an ideal spatial distribution of LSMs and energy transfer events is given according to the results of the conditional average.

Investigation of the interscale interaction between large and small scales (or resolved scales and unresolved subgrid scales) involves spatial filtering [20,21,48,49]. Simple spatial filtering neglects the fact that the coherent structures are anisotropic and inhomogeneous in wall turbulence [50]. As shown in the paper by Lee and Moser [25], the interscale energy transfer spectrum provides details of the donors (negative) and recipients (positive) of energy. In the present paper, the energy-containing large-scale fields and vortex-dominated small-scale fields are decomposed using the energy donor mode as a filter at each flow layer [20]. We focus on the interscale transfer spectra of energy and investigate the flow structures associated with the large scales and small scales. To pursue this, we use the DNS data of turbulent channel flows to perform spectral decomposition and then investigate the spatial organization of the flow structures. The remainder of the paper is organized as follows. The numerical database and spectral energy budget equation used in the present paper are described in Sec. II. Scale decomposition based on interscale energy transfer is introduced in Sec. III. We analyze the spatial coherent structures corresponding to the large scales and small scales in Sec. IV. Finally, we offer an extended discussion and conclusions in Sec. V.

II. NUMERICAL DATA AND FORMULATIONS

A. Data descriptions

In the subsequent descriptions, the streamwise, spanwise, and wall-normal directions are denoted by x^+ , z^+ , and y^+ , and the corresponding velocity components are represented by u^+ , w^+ , and v^+ , respectively. We also use the index u_i ($i = 1, 2, 3$) to indicate the streamwise, wall-normal, and spanwise directions, respectively. The superscript $(\cdot)^+$ represents that the velocity components are normalized using the skin friction velocity u_τ , and the length scale is normalized by the inner length scale ν/u_τ (ν is the kinematic viscosity). The mean velocity is denoted by capital letters as $U_i = \langle u_i \rangle$, and the velocity fluctuations are indicated with primes as $u'_i = u_i - U_i$. Two DNS databases of fully developed turbulent channel flows at $Re_\tau = 180$ and 550 are employed in this paper, where Re_τ is the friction Reynolds number.

Both DNS cases are conducted using a pseudospectral method, where the grid is uniform in the homogeneous directions, while the points are closely concentrated in the wall-normal direction near both walls using cosine mapping. The velocity and pressure are expanded into Fourier series in the streamwise and spanwise directions, and into Chebyshev polynomials in the wall-normal direction. Periodic boundary conditions are employed in both the streamwise and spanwise directions, and the no-slip boundary condition is applied at the wall. The aliasing errors are removed using the $3/2$ rule. Time is advanced with a third-order time splitting method. This code is well validated in turbulent channel flows at various Reynolds numbers [51,52]. The data are stored every ten time steps after the flow is fully developed to a statistically stationary state. The detailed parameters of the two cases are listed in Table I. To obtain smooth spectra, two large datasets with sample numbers of $N_t = 4000$ for $Re_\tau = 180$ and $N_t = 5400$ for $Re_\tau = 550$ are utilized in the present paper.

The profiles of the mean streamwise velocity U^+ , the streamwise turbulence intensity $\langle u'^2 \rangle^+$, the wall-normal turbulence intensity $\langle v'^2 \rangle^+$, and the spanwise turbulence intensity $\langle w'^2 \rangle^+$ are displayed in Figs. 1(a), 1(b), 1(c), and 1(d), respectively. For comparison, standard and reliable DNS data at $Re_\tau = 550$ [54,55] are also presented as black dashed lines. The mean velocity profiles show good

TABLE I. Parameters of the DNS of turbulent channel flows. L_x and L_z represent the computational domain, and Δ_x^+ and Δ_z^+ are the grid spacings in the streamwise and spanwise directions. Δy_{\min}^+ and Δy_{\max}^+ represent the minimum and maximum grid spacing in the wall-normal direction, respectively. N_y denotes the grid number in the wall-normal direction. The parameter Δt^+ represents the simulation time step, and ΔT^+ represents the time interval of the data, which is ten times Δt^+ as the data are stored every ten time steps. N_t denotes the number of snapshots used in the present paper.

Re_τ	L_x/δ	L_z/δ	Δx^+	Δz^+	Δy_{\min}^+	Δy_{\max}^+	N_y	Δt^+	ΔT^+	N_t
180	8π	4π	11.8	5.9	0.054	4.4	64	0.058	0.58	4000
550	4π	2π	12.0	6.0	0.041	6.75	128	0.03	0.30	5400

agreement between our DNS data (red line) and the reference DNS data (black line). The velocity fluctuations of the reference DNS are slightly larger than those of the data used in the present paper. This weak difference may be caused by the relatively small computational domain used in the case of $Re_\tau = 550$.

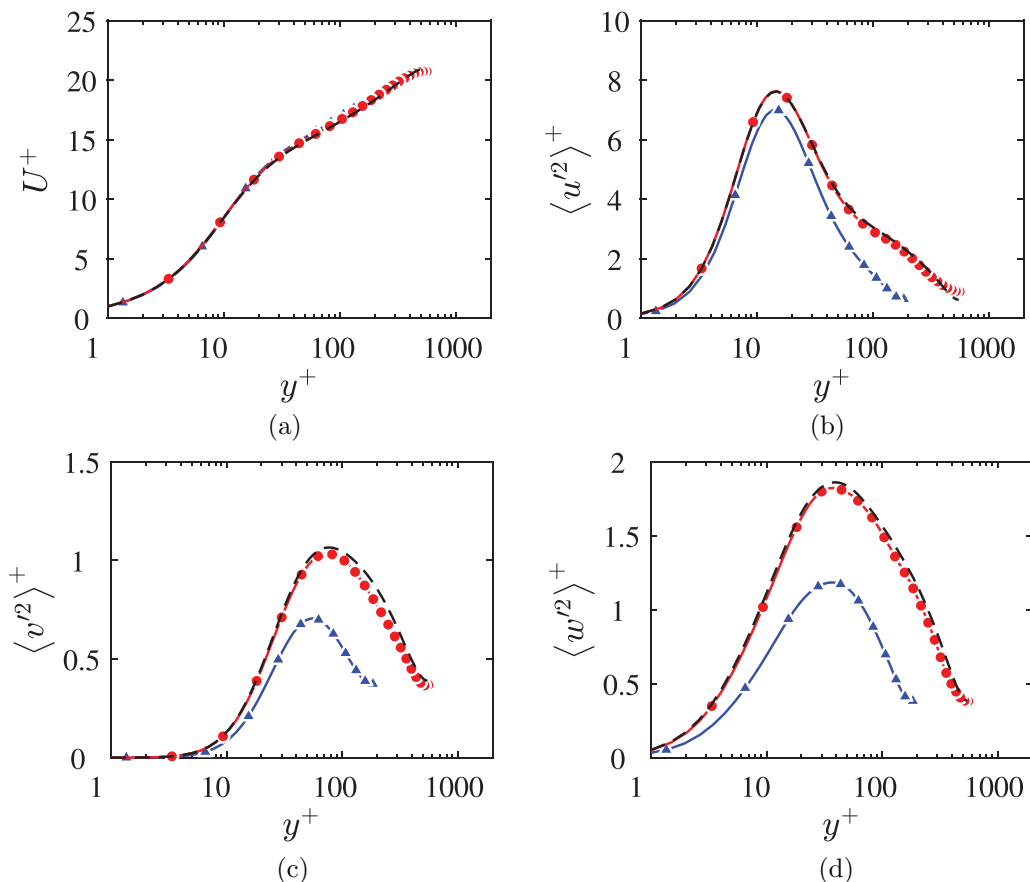


FIG. 1. Statistical profiles of DNS datasets: (a) mean streamwise velocity U^+ ; (b) streamwise turbulence intensity $\langle u'^2 \rangle^+$; (c) wall-normal turbulence intensity $\langle v'^2 \rangle^+$; (d) spanwise turbulence intensity $\langle w'^2 \rangle^+$. The blue and red lines correspond to $Re_\tau = 180$ and 550 , respectively. The black dashed line represents the DNS results downloaded from Ref. [53]; for details on the simulation, please refer to Álamo and Jiménez [54] and Hoyas and Jiménez [55].

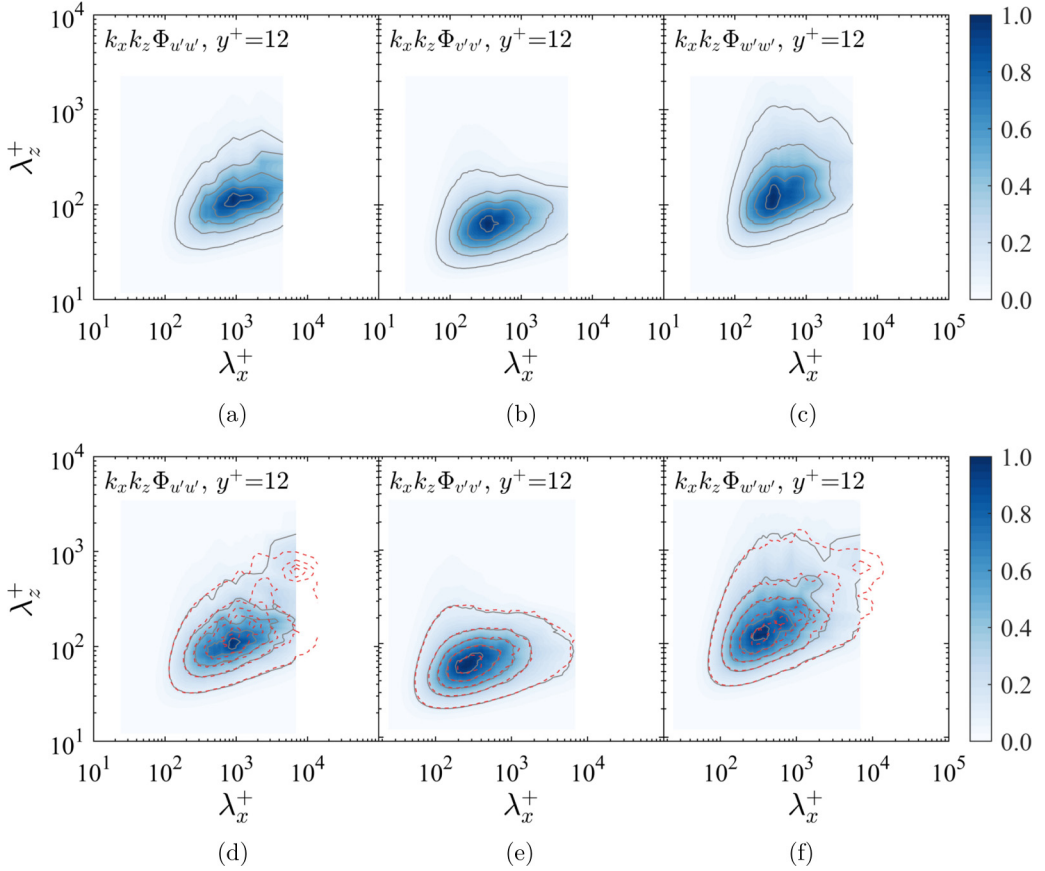


FIG. 2. Premultiplied two-dimensional spectra of u' (a), (d), v' (b), (e), and w' (c), (f) at $y^+ = 12$ for Reynolds numbers $Re_\tau = 180$ (a)–(c) and 550 (d)–(f). The parameters k_x and k_z are the streamwise and spanwise wave numbers, respectively. The solid gray lines correspond to contour levels from 0.1 to 0.9 with an interval of 0.2. For comparison, the spectra computed at $Re_\tau = 550$ with a larger domain of $L_x = 8\pi\delta$ and $L_z = 3\pi\delta$ are also presented as the red dashed lines. The spectra are normalized by the maximum magnitude and filtered by adopting a bandwidth moving filter of 20% [56].

Figure 2 shows the premultiplied two-dimensional energy spectra of u' (a), (d), v' (b), (e), and w' (c), (f) at $y^+ = 12$ for Reynolds numbers $Re_\tau = 180$ (a)–(c) and 550 (d)–(f). In the near-wall region at $y^+ = 12$, the energy peak of the streamwise velocity fluctuation u' resides at $\lambda_x^+ \approx 1000$ and $\lambda_z^+ \approx 100$, which is strongly associated with the elongated streaks generated by the near-wall cycle. The high-energy region of v' is distributed at $\lambda_x^+ \approx 300$ and $\lambda_z^+ \approx 70$ and that of w' is at $\lambda_x^+ \approx 350$ and $\lambda_z^+ \approx 100$. The Reynolds number effect has little influence on the near-wall dominant coherent structures. For comparison, the spectra computed using the DNS data with a larger computational domain of $L_x = 8\pi\delta$ and $L_z = 3\pi\delta$ are also displayed as the red dashed lines in Figs. 2(d)–2(f). The biggest difference is that the second energy peak at large scales ($\lambda_x^+ \approx 7000$ and $\lambda_z^+ \approx 600$) is resolved by the case of larger computational domain. This suggests that the near-wall structures are modulated by the outer large scales, as proposed by Marusic *et al.* [37]. These superposition and modulation effects become stronger as the Reynolds number increases [25,38]. From this comparison at $Re_\tau = 550$, we found that the streamwise computational domain of $4\pi\delta$ is not enough to resolve the largest scales in turbulence. However, on the one hand, the spectra corresponding to the near-wall dominant coherent structures are exactly the same. On the

other hand, the energy of the second large-scale peak is much weaker than that of the energy peak of the near-wall dominant coherent structures. Therefore, this limitation of computational domain has little influence on the decomposition proposed in the present paper. In addition, the gray solid lines present good agreement with the red dashed lines in Fig. 2(e); this implies that the spectra of v' at $y^+ = 12$ are not affected by the computational domain. Meanwhile, the second energy peak at large scales is not observed from the spectra of v' .

B. Spectral energy budget equation in a channel flow

For fully developed channel flows, the budget equation of energy spectra can be simplified in the streamwise and spanwise directions, i.e., the homogeneous plane parallel to the wall [13,22]. We consider the two-dimensional spectral energy budget equation directly deduced from the Fourier transform of the Navier-Stokes equation [13,17,18,20] instead of the two-point correlation function of the velocity fluctuations [21,22,25]. The Fourier transform of the velocity fluctuation component u'_i in the wall-parallel plane is given as

$$u'_i(x, y, z, t) = \int_{-\infty}^{\infty} \int_{-\infty}^{\infty} \widehat{u}'_i(k_x, y, k_z, t) e^{ik_x x} e^{ik_z z} dk_x dk_z, \quad (1)$$

where $\widehat{(\cdot)}$ represents the two-dimensional Fourier transform coefficient and k_x and k_z are the streamwise and spanwise wave numbers, respectively. For brevity, $\widehat{u}'_i(k_x, y, k_z, t)$ is abbreviated as \widehat{u}'_i , and its complex conjugate is denoted by \widehat{u}'_i^* .

The spectral form of the energy budget equation for a turbulent channel flow is given as follows [13]:

$$\begin{aligned} \frac{\partial \widehat{E}}{\partial t} = & \underbrace{-2\nu k^2 \widehat{E}}_{\epsilon_p} + \underbrace{\nu \frac{\partial^2 \widehat{E}}{\partial x_2^2}}_{\phi_v} - \underbrace{\nu \left\langle \frac{\partial \widehat{u}'_i^*}{\partial x_2} \frac{\partial \widehat{u}'_i}{\partial x_2} \right\rangle}_{\epsilon_y} \\ & - \underbrace{\mathcal{R} \left\langle \widehat{u}'_1^* \widehat{u}'_2 \frac{\partial U_1}{\partial x_2} \right\rangle}_{\Pi} - \underbrace{\mathcal{R} \left\langle \widehat{u}'_i^* \frac{\partial (\widehat{u}'_i \widehat{u}'_j)}{\partial x_j} \right\rangle}_{T} - \underbrace{\frac{\partial}{\partial x_2} \mathcal{R} \{ \widehat{u}'_2^* \widehat{p}' \}}_{\phi_p}. \end{aligned} \quad (2)$$

Here, $\langle \cdot \rangle$ refers to the time averaging, k^2 is equal to $k_x^2 + k_z^2$, and \mathcal{R} denotes the real part. \widehat{E} is the spectral TKE, which is calculated as $\frac{1}{2} \langle \widehat{u}'_i \widehat{u}'_i^* \rangle$. On the right-hand side of Eq. (2), ϵ_p , ϕ_v , ϵ_y , Π , T , and ϕ_p represent in-plane dissipation, interplane viscous diffusion, interplane dissipation, shear-induced turbulence production, nonlinear energy transfer, and pressure diffusion, respectively. According to Mizuno [17], the nonlinear term T can be rewritten as the summation of two parts as

$$T = \underbrace{-\mathcal{R} \left\langle \widehat{u}'_i^* \frac{\partial (\widehat{u}'_i \widehat{u}'_j)}{\partial x_j} \right\rangle - \frac{1}{2} \frac{\partial \langle \widehat{u}'_i^* (\widehat{u}'_i \widehat{u}'_2) \rangle}{\partial x_2}}_{T^{\parallel}} - \underbrace{\frac{1}{2} \mathcal{R} \left\langle \frac{\partial \widehat{u}'_i^* (\widehat{u}'_i \widehat{u}'_2) \rangle}{\partial x_2} \right\rangle}_{T^{\perp}}. \quad (3)$$

The in-plane nonlinear transfer term T^{\parallel} represents the energy transport between scales; therefore, this term can also be called interscale energy transfer [17,25]. The integration of the term T^{\parallel} over the whole scale space yields zero; therefore, this term has no contribution to the total energy budget [17,20]. The interplane term T^{\perp} represents the energy transfer in the wall-normal direction, as shown in Fig. 3. At $y^+ = 15$, T^{\perp} is almost negative at every scale; however, there are positive regions at $y^+ = 5$ and 70. This means that the energy at $y^+ = 15$ is transferred into the upward and downward directions. The present paper focuses on the interscale energy transfer associated with the energy cascade; for a discussion on spatial energy transfer, please refer to the paper by Mizuno [17].

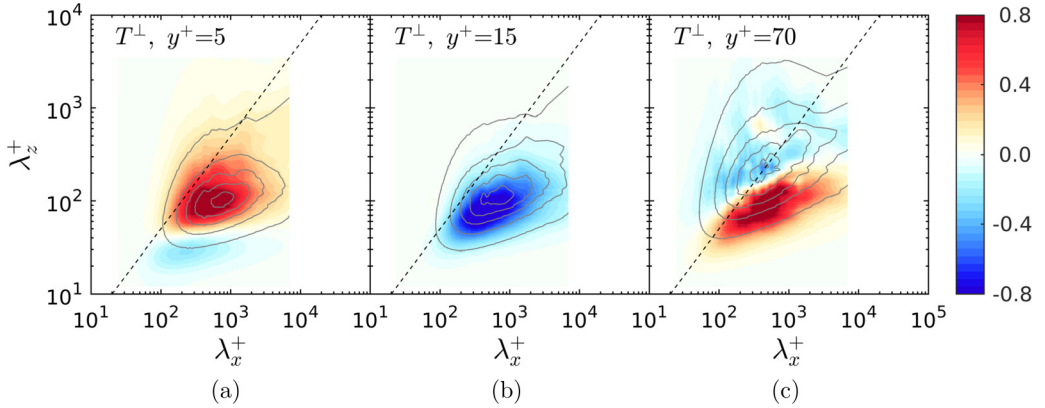


FIG. 3. Premultiplied two-dimensional spatial transfer spectra at different y^+ for $\text{Re}_\tau = 550$. The solid gray curves represent the corresponding TKE spectra, and the contour values increment by 0.2, starting with 0.1 and ending with 0.9. The black dashed lines represent $\lambda_x^+ = 2\lambda_z^+$. The spectra are normalized by the maximum magnitude and filtered by adopting a bandwidth moving filter of 20% [56].

III. SCALE DECOMPOSITION BASED ON INTERSCALE ENERGY TRANSFER

A. Interscale energy transfer

We first investigate the features of the production spectra, as shown in Fig. 4. The solid gray contour lines represent the corresponding TKE spectra, and the black dashed lines represent $\lambda_x^+ = 2\lambda_z^+$. The energy production has most of its content for $\lambda_x^+ > 2\lambda_z^+$ and shows streamwise-elongated flow structures. The region of positive production is coincident with that of the high TKE spectra, especially for $y^+ \geq 15$. For $y^+ = 5$ as shown in Figs. 4(a) and 4(b), the streamwise and spanwise wavelengths corresponding to the production peak are slightly smaller than those of the TKE spectra. The most interesting aspect is that there is a negative region for production. This feature has also been reported in the paper by Lee and Moser [25]. The negative peaks almost occur at wavelengths of $(\lambda_x^+, \lambda_z^+) = (200, 300)$ and are elongated in the spanwise direction. However, the magnitude of the negative production is much less than that of the positive production. The boundary between the negative region and the positive region is $\lambda_x^+ = 2\lambda_z^+$ in the near-wall region. From the results of $\text{Re}_\tau = 180$ and 550, we find that the Reynolds number effect on near-wall energy production can be ignored.

The interscale energy transfer spectra T^{\parallel} at several y positions near the wall for different Reynolds numbers are shown in Fig. 5. It is obvious that the spectra T^{\parallel} are characterized by a negative region and a positive region. As proposed by Lee and Moser [25], the negative region is referred to as the donor mode, and the positive region is referred to as the recipient mode. The energy is transferred from the donor mode to the recipient mode. The donor region presents streamwise-elongated structures since this region is below the black dashed line. The donor peak at $y^+ = 15$ appears at $\lambda_x^+ \approx 1000$ and $\lambda_z^+ \approx 100$, which is consistent with the scales of the near-wall streaks [57–60]. Both spanwise and streamwise scales increase with increasing y^+ . With Re_τ increasing, the donor regions present weak Reynolds number dependence. Compared with the production spectra, the donor region is highly correlated with the positive production region which is the true source of turbulent energy except that the donor region is smaller than that of production [25].

The energy recipient region in the near-wall region is more interesting. One dominant feature is that the recipient region is divided into two parts in accordance with the two recipient peaks (at $y^+ = 15$): the spanwise-elongated recipient region, which contains a peak at $(\lambda_x^+, \lambda_z^+) \approx (300, 200)$, and the streamwise-elongated recipient region, which contains a peak at $(\lambda_x^+, \lambda_z^+) \approx (150, 40)$. These

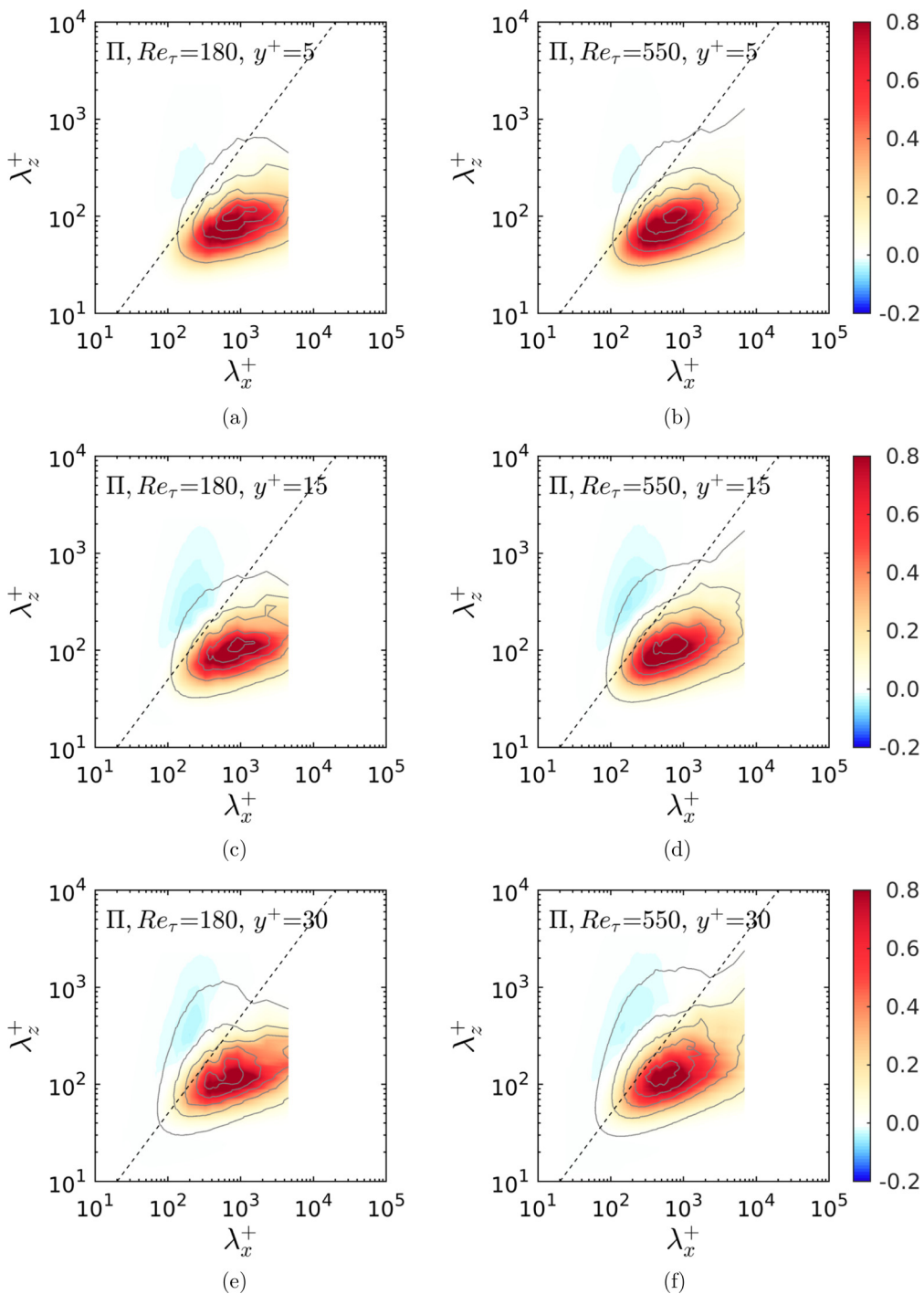


FIG. 4. Premultiplied two-dimensional production spectra at $y^+ = 5$ (a), (b), 15 (c), (d), and 30 (e), (f) for $Re_\tau = 180$ (a), (c), (e) and 550 (b), (d), (f). The solid gray curves represent the corresponding TKE spectra, and the contour values increment by 0.2, starting with 0.1 and ending with 0.9. The black dashed lines represent $\lambda_x^+ = 2\lambda_z^+$. The spectra are normalized by the maximum magnitude and filtered by adopting a bandwidth moving filter of 20% [56].

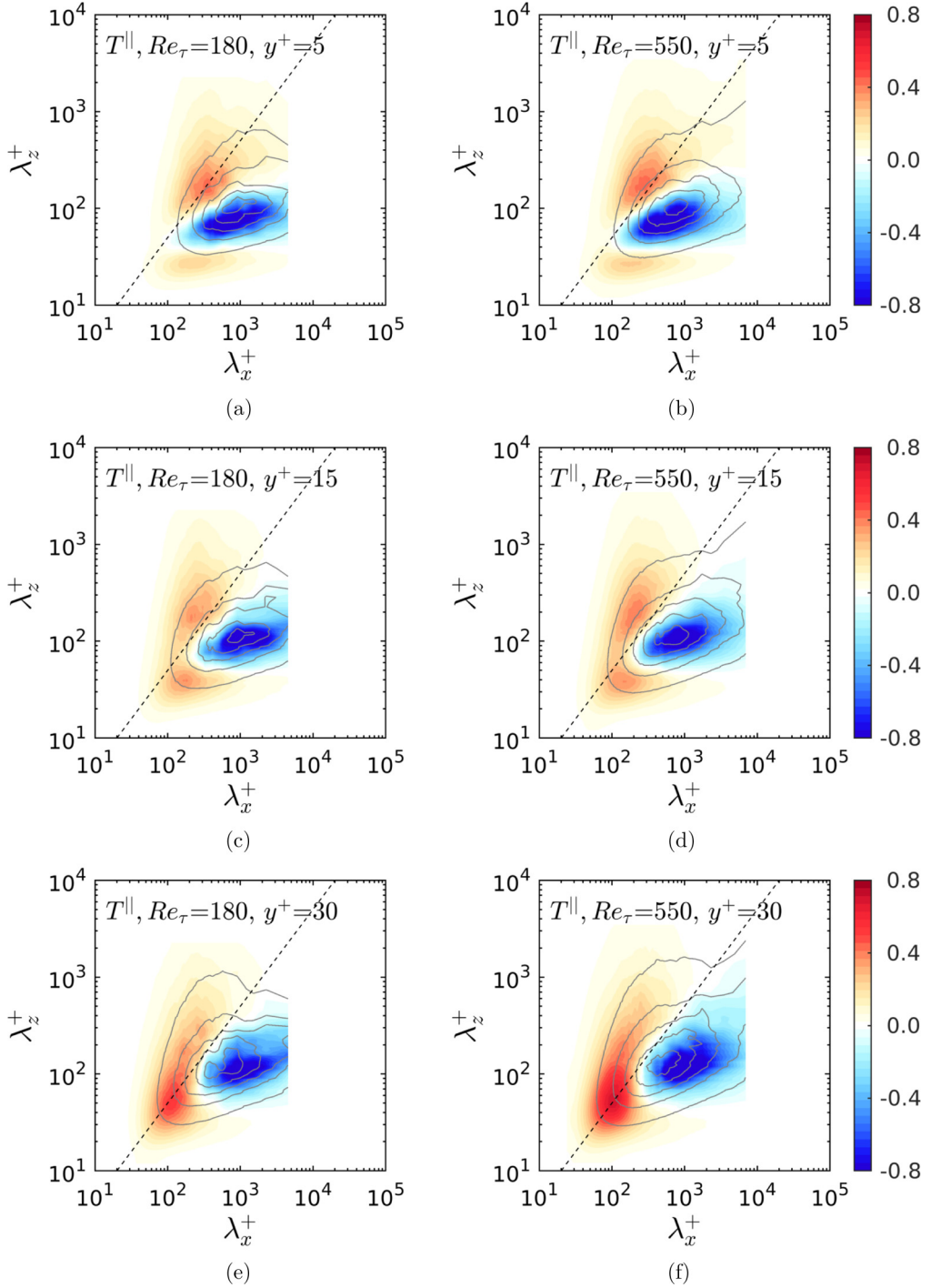


FIG. 5. Premultiplied two-dimensional interscale transfer spectra at $y^+ = 5$ (a), (b), 15 (c), (d), and 30 (e), (f) for $Re_{\tau} = 180$ (a), (c), (e) and 550 (b), (d), (f). The solid gray curves represent the corresponding TKE spectra, and the contour values increment by 0.2, starting with 0.1 and ending with 0.9. The black dashed lines represent $\lambda_x^+ = 2\lambda_z^+$. The spectra are normalized by the maximum magnitude and filtered by adopting a bandwidth moving filter of 20% [56].

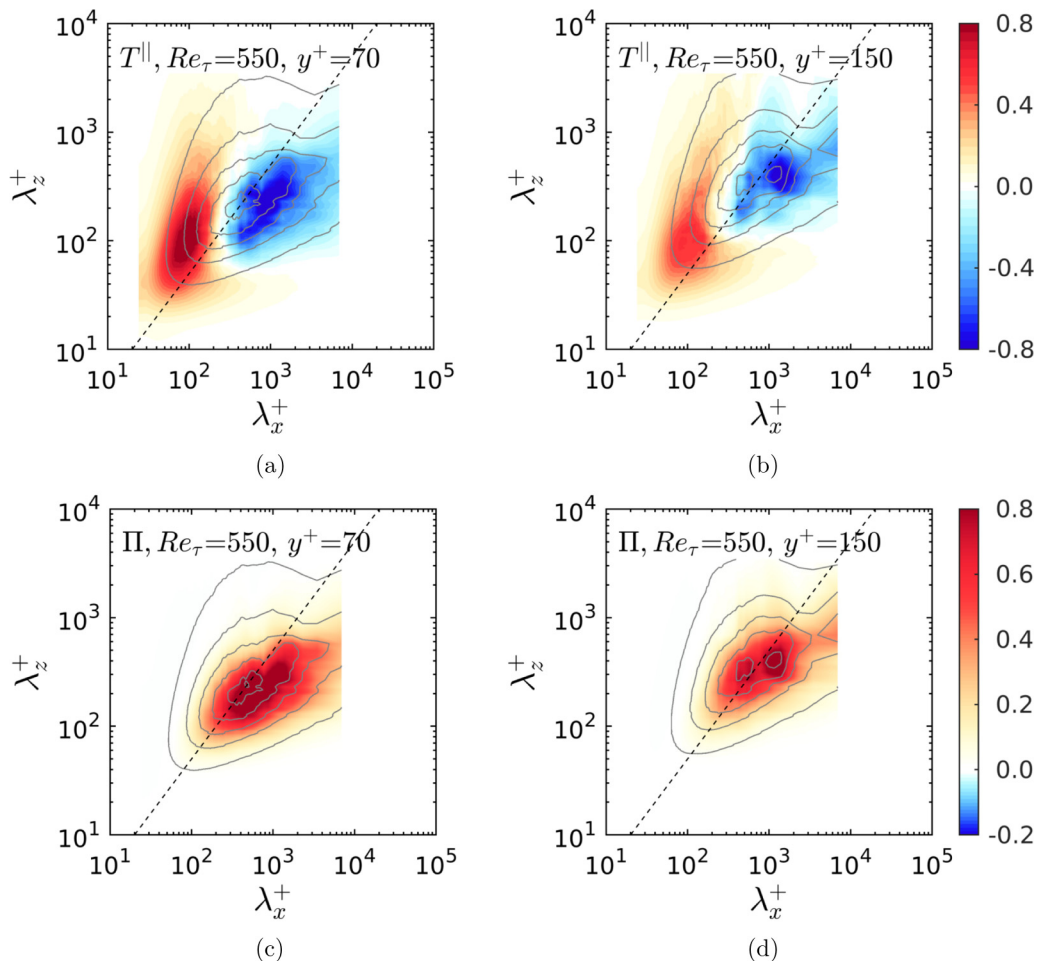


FIG. 6. Premultiplied interscale transfer spectra (a), (b) and production spectra (c), (d) in the outer layer of $y^+ = 70$ (a), (c) and 250 (b), (d) at $Re_{\tau} = 550$. The solid gray curves represent the corresponding TKE spectra, and the contour values increment by 0.2, starting with 0.1 and ending with 0.9. The black dashed lines represent $\lambda_x^+ = 2\lambda_z^+$. The spectra are normalized by the maximum magnitude and filtered by adopting a bandwidth moving filter of 20% [56].

peak locations vary with the wall-normal location but are essentially unaffected by the Reynolds number. These two recipient peaks are distributed on both sides of the donor region in the spanwise direction, which implies that the energy is transferred to smaller scales (forward energy cascade) as well as larger scales (backward energy cascade) in the spanwise direction. As seen from Fig. 5, the dominant spanwise scale λ_z^+ is approximately 100 from the TKE spectra. However, the backward energy cascade can generate much larger spanwise flow structures [25]. Moreover, at $y^+ = 15$, the spanwise-elongated recipient region is highly relevant to the negative production region for different Re_{τ} . The intrinsic connection between the backward energy cascade and negative production is not yet clear. The streamwise-elongated recipient region represents very narrow streaks in the near-wall region, which is also not the dominant flow structure in wall-bounded turbulence. The energy production in this region is almost zero.

Figure 6 presents the interscale transfer spectra and the production spectra at the outer region of $y^+ = 70$ and 250 for $Re_{\tau} = 550$. There is no negative region in the energy production, which means

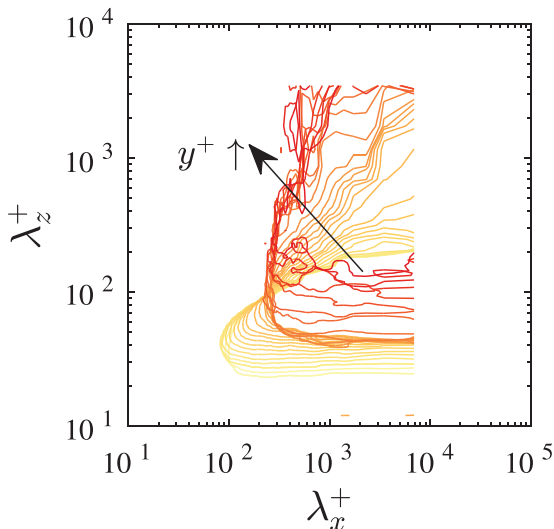


FIG. 7. The zero-crossing boundary in the interscale transfer spectra at $\text{Re}_\tau = 550$. The wall-normal position y^+ increases from 1 to 250 as the line color changes from yellow to red.

the negative production arises in the near-wall region only. The donor region is still consistent with the region of production, and both present streamwise-elongated modes. Different from the recipient region near the wall, only one peak at $(\lambda_x^+, \lambda_z^+) \approx (100, 100)$ occurs in the recipient region. In addition, no backward energy cascade is observed from the T^{\parallel} spectra. The energy is redistributed from the streamwise-elongated scales to the nearly isotropic scales.

B. Scale decomposition

As discussed in the previous section, the scale space is divided into the donor region and recipient region. The former contains energetic streamwise-elongated large scales. As proposed by Wang *et al.* [20], the zero-crossing boundary in the T^{\parallel} spectrum can be used to separate the large scales (defined as the donor scales) and the small scales (defined as the recipient scales) at each flow layer. Figure 7 displays the variation trend of the zero-cross boundary as y^+ increases from 1 to 250 at $\text{Re}_\tau = 550$. Generally, the shape of the boundary changes from triangle to rectangle as y^+ increases and moves toward the region of large scales. Another feature is that the boundary curve becomes coarser at higher y^+ because the large scales require more samples to converge the statistical results, which has been discussed in Sec. II A. In practice, the spectral mask is slightly Gaussian smoothed to avoid the discontinuity in the wall-normal direction. The large-scale flow field, which is actually the energy donor scale, is obtained through inverse Fourier transform of the two-dimensional velocity spectrum sharp-filtered by the donor region. The small scales are obtained by subtracting the large scales from the original DNS fields. It is meaningful to use these filters, which vary with y^+ and are anisotropic in the streamwise and spanwise directions, since the most energetic coherent structures are highly anisotropic [50].

The flow structures of the original DNS data, the large-scale field, and the small-scale field are visualized in Fig. 8 from top to bottom, and the Reynolds number Re_τ is 550. The isosurfaces colored based on the wall-normal height y^+ indicate low-speed streaks of $u' = -1.5$, and the isosurfaces colored by the streamwise fluctuation velocity u' represent vortical structures identified by the Q criterion, where Q denotes the vortex identification criterion estimated as the second invariant of the velocity gradient tensor. The streamwise extent of these figures is approximately 12δ , and the spanwise length scale is approximately 3δ . Regarding the flow structures of the original DNS

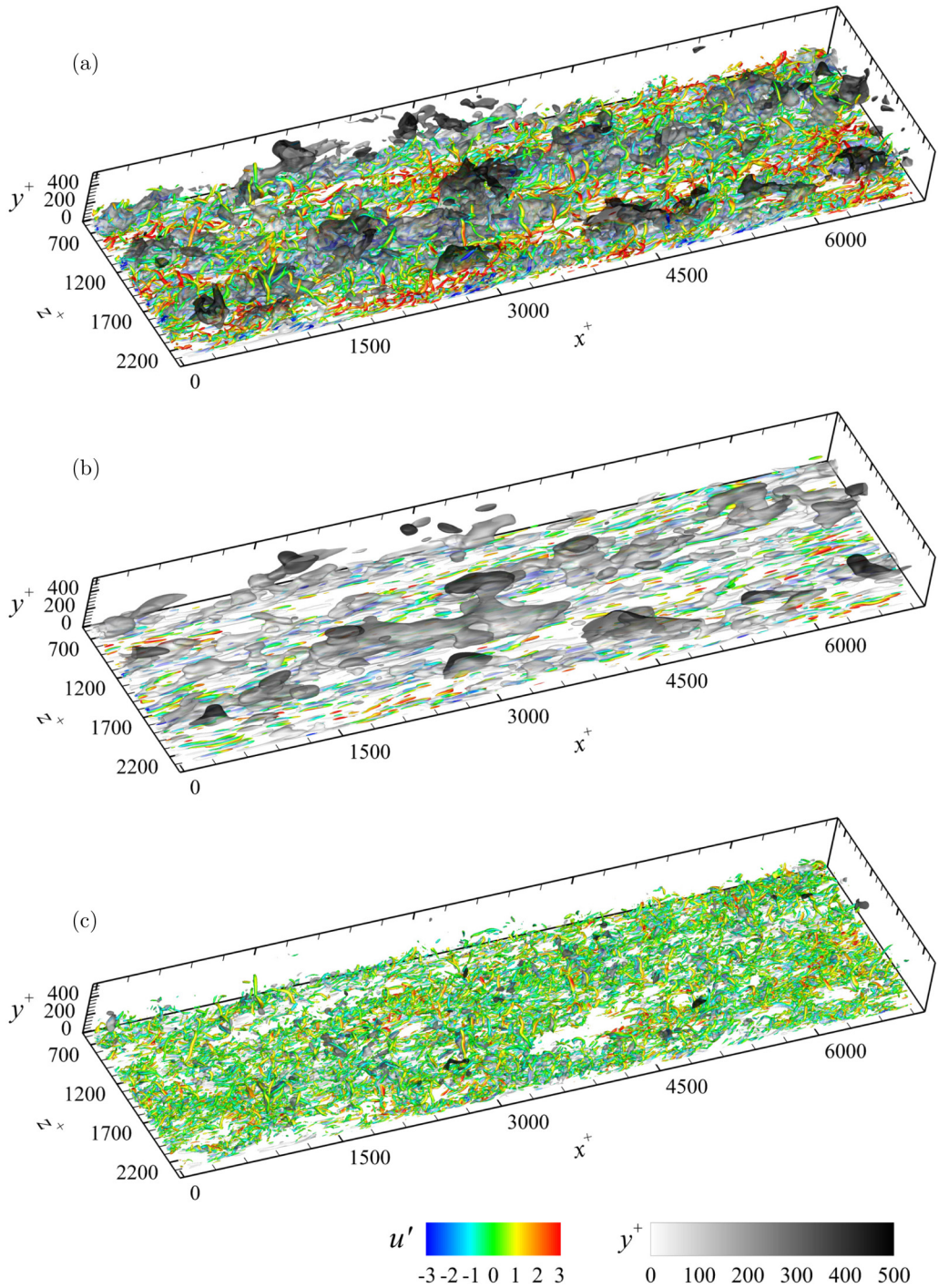


FIG. 8. Visualization of vortices and low-speed streaks for the original DNS data (a), the large-scale field (b), and the small-scale field (c) at a Reynolds number of $Re_\tau = 550$. The isosurfaces colored based on the wall-normal height y^+ indicate low-speed streaks of $u' = -1.5$, and the isosurfaces colored by the streamwise fluctuation velocity u' represent vortical structures identified by the Q criterion with $Q = 0.006$.

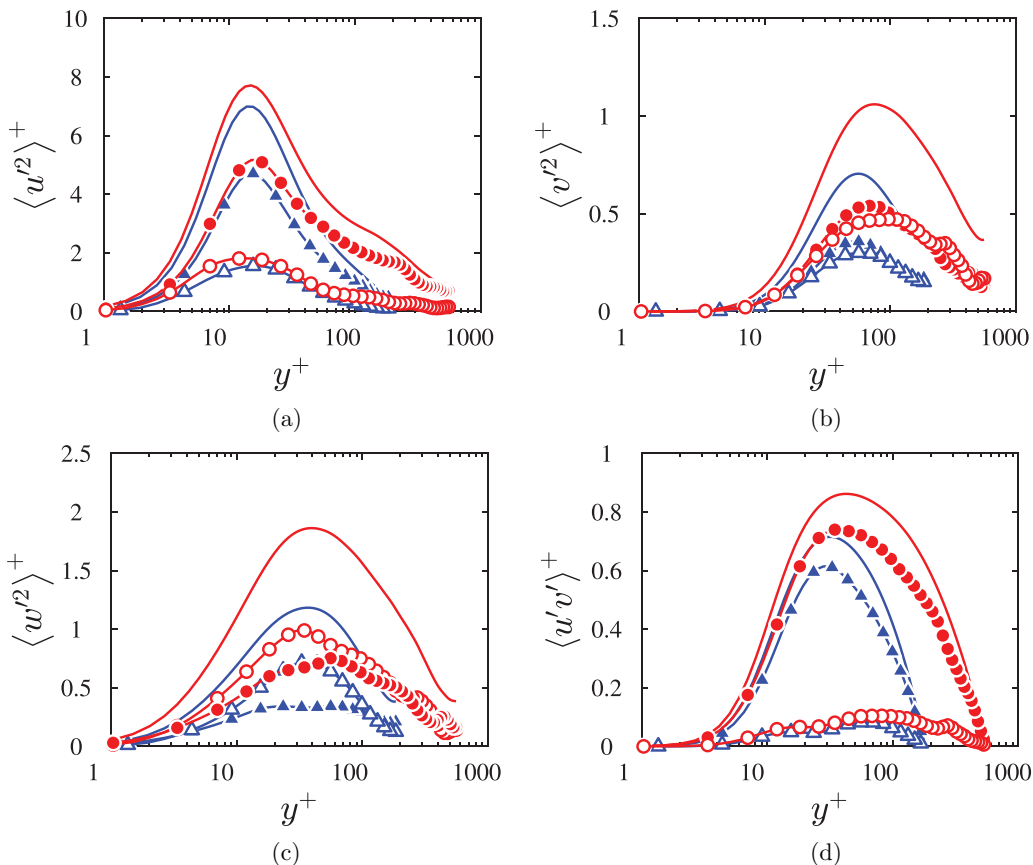


FIG. 9. Statistical profiles of the large scales (the solid symbols) and the small scales (the hollow symbols) at $Re_\tau = 180$ (blue) and 550 (red). The solid lines denote the profiles of the original DNS data.

data, the low-speed structures present characteristics of LSMs and VLSMs and are surrounded by many hairpin-like vortices. Moreover, the low-speed structures extend down to the near-wall region and up to the whole boundary layer. The legs of hairpins become quasi-streamwise vortices in the buffer layer and induce low-momentum fluid upwards. The heads of hairpins located in the outer layer are characterized by transverse (spanwise) vortices rotating in the same direction as the mean circulation [2]. The large-scale field shown in Fig. 8(b) is characterized by streaks and streamwise vortices on the flank. This pattern is consistent with the near-wall self-sustaining process in which the streak is generated through the lift-up effect of the streamwise vortices, and then the streak nonlinear instability forms new vortices. For the small-scale field in Fig. 8(c), the vortical structures are almost the same as those in the original flow fields, i.e., the isosurfaces of the Q criterion in Figs. 8(c) and 8(a) are similar. Under the same thresholds of isosurfaces, we cannot observe the large-scale flow structures in Fig. 8(c). From this flow visualization, we would like to offer two remarks. First, vortices identified based on the velocity gradient mainly represent locally small-scale structures [61]. Large-scale structures are suitable to be characterized by velocity. Second, the large-scale structures may be related to the quasi-streamwise vortices, as shown in Fig. 8(b), rather than the hairpin-like vortices.

The Reynolds stresses of the large-scale fields (the solid symbols) and the small-scale fields (the hollow symbols) at $Re_\tau = 180$ and 550 are presented in Fig. 9. The Reynolds stresses $\langle u'^2 \rangle^+$ and $\langle u'v' \rangle^+$ of the large scales are much larger than those of the small scales, whereas the Reynolds

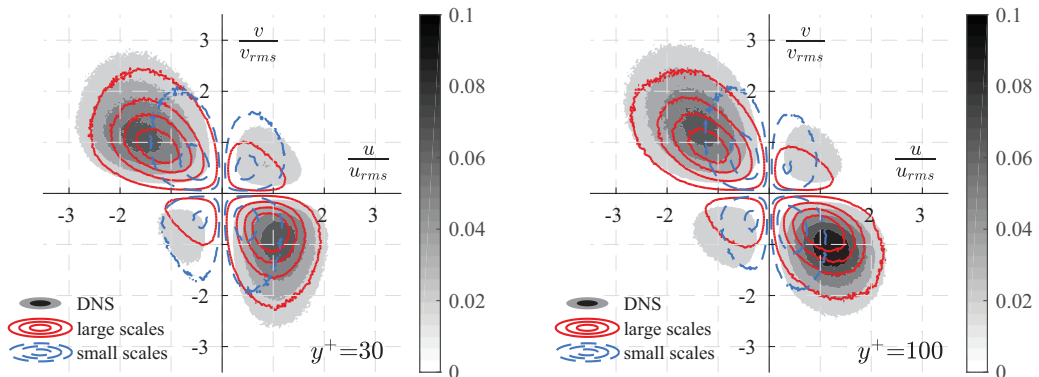


FIG. 10. Reynolds shear stress weighted joint PDF of u^+ and v^+ at $y^+ = 30$ (a) and 100 (b) for $Re_\tau = 550$. The gray colors represent the PDF of raw DNS data, and the red and blue contours represent the PDF of large scales and small scales, respectively. The contour levels are from 0.01 to 0.1 in a step of 0.03. The velocity is scaled by the root mean square of the original DNS velocity at this location.

stresses $\langle v^2 \rangle^+$ and $\langle w^2 \rangle^+$ are slightly smaller than those of the small scales. The wall-normal position of the peak of $\langle u'^2 \rangle^+$ is consistent with the original DNS profile. The large-scale structures contribute approximately 65% of the streamwise TKE and 80% of the Reynolds shear stress. These values are higher than the result proposed by Balakumar and Adrian [62], where it is stated that 40–65% of the TKE and 30–50% of the Reynolds shear stress are carried by VLSMs in channel flows. The Reynolds shear stress $\langle u'v' \rangle^+$ is also related to the production term of the TKE. The large-scale flow fields dominate the production of the TKE.

Quadrant analysis [63] is further used to determine the Reynolds shear stress contribution of large and small scales. Figure 10 shows the Reynolds shear stress weighted joint probability distribution function (PDF) of u^+ and v^+ at $y^+ = 30$ (a) and 100 (b) for $Re_\tau = 550$. The gray colors, red contours, and blue contours represent the weighted PDF of the original DNS data, large scales, and small scales, respectively. It is clear that the large scales are dominated by $Q2$ ($u^+ < 0, v^+ > 0$, ejection) and $Q4$ ($u^+ > 0, v^+ < 0$, sweep) events, which is similar to the result of raw DNS data. The $Q2$ and $Q4$ events result in momentum transfer in the wall-normal direction, which results in a positive contribution to the Reynolds shear stress. For the small scales indicated by the blue contours, the contributions to $Q1$ ($u^+ > 0, v^+ > 0$, outward interaction) and $Q3$ ($u^+ < 0, v^+ < 0$, wallward interaction) events are comparable to $Q2$ and $Q4$ events. Therefore, the Reynolds shear stress at small scales is much less than that at large scales, as shown in Fig. 9.

IV. FLOW STRUCTURES

Up to now, the flow field has been decomposed into large scales and small scales based on interscale transfer spectra without any artificial or subjective thresholds. In this section, proper orthogonal decomposition (POD) and linear stochastic estimation (LSE) are used to extract the dominant flow structures of the large-scale fields and the small-scale fields. There are two objectives. First, we seek the flow structures associated with the donor modes in the interscale transfer spectra. Second, we aim to assess the similarity of the flow structures appearing in the near-wall region and outer region.

A. Proper orthogonal decomposition

To further visualize the large-scale flow fields, POD, which is used to extract the most energetic coherent structures in the turbulence [22,64], is applied to the two-dimensional three-component

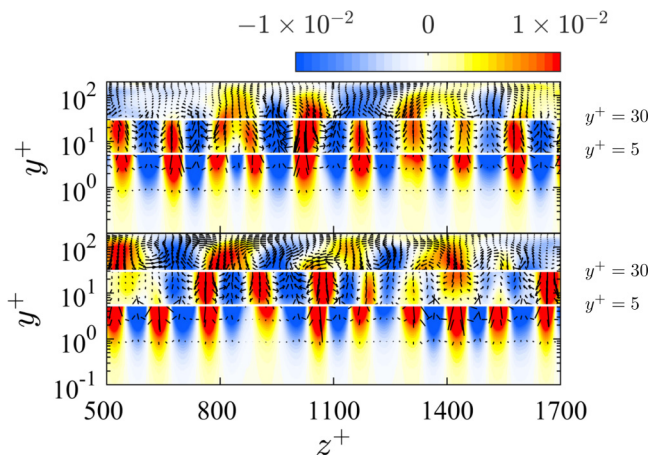


FIG. 11. The first two POD modes (the upper panel is for the first POD mode, and the bottom panel is for the second POD mode) of the large-scale flow fields in the regions of $0 \leq y^+ \leq 5$, $5 \leq y^+ \leq 30$, and $30 \leq y^+ \leq 180$ using the cross stream view. Here, the Reynolds number Re_τ is 180. The contour represents the low- and high-speed (blue and red) u' component of the streaks, and the arrows denote the $v' - w'$ components. Only part of the spanwise range is shown in this figure for clarity.

(2D3C) velocity fields at the $y^+ - z^+$ plane. These 2D3C fields are generated by randomly slicing the large-scale flow data in the direction of spatial x and temporal t . POD provides a series of orthogonal modes for the spatial structures. These modes are computed by eigenanalysis of the two-point spatial covariance of the fluctuating flow and ordered according to the contribution to the energy of the flow. In the present paper, we use the snapshot method introduced by Sirovich [65] to effectively compute the modes. On the one hand, the scale of the structures increases as the wall-normal location y^+ increases in accordance with Townsend's attached eddy hypothesis [8,66]. On the other hand, the magnitude of velocity fluctuation also varies with y^+ , as shown in Fig. 1. Therefore, it is better to perform POD at different wall-normal regions to obtain local optimal modes. We demarcated the wall-normal regions in accordance with the classical wall layers, as given in Pope [10]. For $Re_\tau = 180$, the flow fields are divided into three parts of $0 \leq y^+ \leq 5$ (viscous sublayer), $5 \leq y^+ \leq 30$ (buffer layer), and $30 \leq y^+ \leq 180$ (outer layer). For $Re_\tau = 550$, the flow fields are divided into four parts of $0 \leq y^+ \leq 5$ (viscous sublayer), $5 \leq y^+ \leq 30$ (buffer layer), $30 \leq y^+ \leq 120$, and $120 \leq y^+ \leq 550$. The first two POD modes of the large scales at $Re_\tau = 180$ are shown in Fig. 11; the near-wall structures can be clearly identified by using a log-scale y axis. The contour represents the low- (blue) and high-speed (red) u' component of the streaks, and the arrows denote the $v' - w'$ components. In the near-wall region of $0 \leq y^+ \leq 30$, we observe a group of regular high- and low-speed streaks aligned along the spanwise direction. The spanwise wavelength is approximately 120. The streamwise velocity streaks are flanked by a pair of counter-rotating streamwise vortices. Positive wall-normal velocity is related to the low-speed streaks through carrying low-momentum fluid toward a higher wall-normal position. The negative wall-normal velocity is related to the high-speed streaks through the opposite process. This coherent structure is a typical representation of the near-wall cycle. The first mode and second mode represent the same flow structure. The difference between these paired modes is the phase in the spanwise direction, which is caused by the meandering of streaks. In the outer region ($y^+ \geq 30$), the flow pattern is very similar to that in the near-wall region except that the spanwise scale of the large coherent motion is $\lambda_z^+ \approx 300$ and the vortex position is at $y^+ \approx 70$.

The POD results for $Re_\tau = 550$ are also presented in Fig. 12. The large-scale coherent structure still presents a streak-vortex pattern, and the spanwise scale increases with increasing y^+ . Due to the modulation, randomness, and asymmetry of the flow structures as Re_τ increases, however, the flow

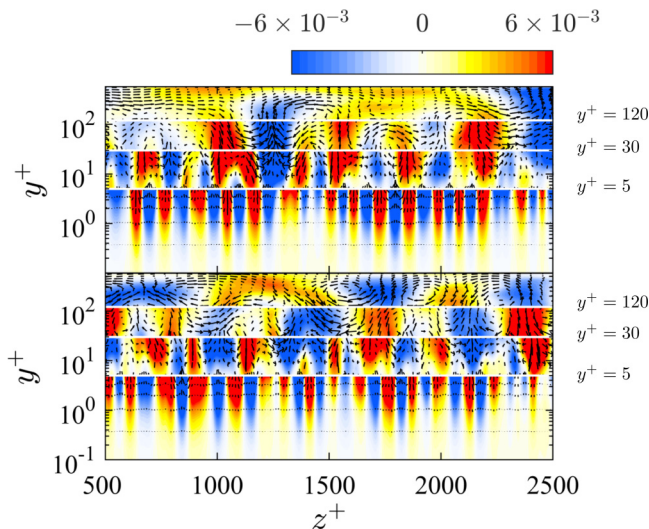


FIG. 12. The first two POD modes (the upper panel is for the first POD mode, and the bottom panel is for the second POD mode) of the large-scale flow fields in the regions of $0 \leq y^+ \leq 5$, $5 \leq y^+ \leq 30$, $30 \leq y^+ \leq 120$, and $120 \leq y^+ \leq 550$ using the cross stream view. Here, the Reynolds number is $Re_\tau = 550$. The contours represent the low- and high-speed (blue and red) u' components of the streaks, and the arrows denote the $v' - w'$ components. Only part of the spanwise range is shown in this figure for clarity.

pattern in Fig. 12 is more disordered than that of $Re_\tau = 180$. It is better to apply the spatial-temporal POD [67] or spectral POD [68,69] to extract coherent structures at high Reynolds numbers, which is beyond the scope of the present paper.

Based on these large-scale POD results, we provide two remarks on the decomposition. First, the formation of the negative interscale energy transfer spectra is ascribed to coherent flow structures consisting of streaks and streamwise vortices. Second, the POD mode of the large scales in the outer region also consists of streaks and streamwise vortices, the length scales of which are much larger than those in the near-wall region. This outer flow structure is consistent with the invariant solutions computed using an overdamped large-eddy simulation in turbulent channel flow [42,70]. The similarity between the near-wall region and outer region may suggest the existence of a self-sustaining process for the large scales in the outer region.

B. Conditionally averaged flow fields

To extract the three-dimensional structures, LSE, a kind of conditional averaging technique, is used to extract the mean and main vortical structures around a reference point according to the given events [71,72]. Conditional averaging can be regarded as a cross-correlation of two signals, one of which defines the events, and the other is the data to be averaged. By supposing that the conditional average $\langle u'_i | E \rangle$ is a linear function of the event E , $\langle u'_i | E \rangle$ can be obtained using a linear mean-square estimation as [73,74]

$$u'_i(r_x, y, y_{\text{ref}}, r_z) = \frac{\langle u'_i(x + r_x, y, z + r_z) E(x, y_{\text{ref}}, z) \rangle}{\langle E(x, y_{\text{ref}}, z)^2 \rangle} E(x, y_{\text{ref}}, z). \quad (4)$$

Here, the parameters r_x and r_z are the streamwise and spanwise distances from the events, respectively, y_{ref} is the reference wall-normal position, and E represents the event or condition. To investigate the contribution of the large-scale fields and the small-scale fields to the low-speed velocity streaks, the event E is chosen as the low-speed velocity of $u' \leq -u'_{\text{rms}}$ in the original DNS fields, where u'_{rms} denotes the root mean square (rms) streamwise velocity at the reference position.

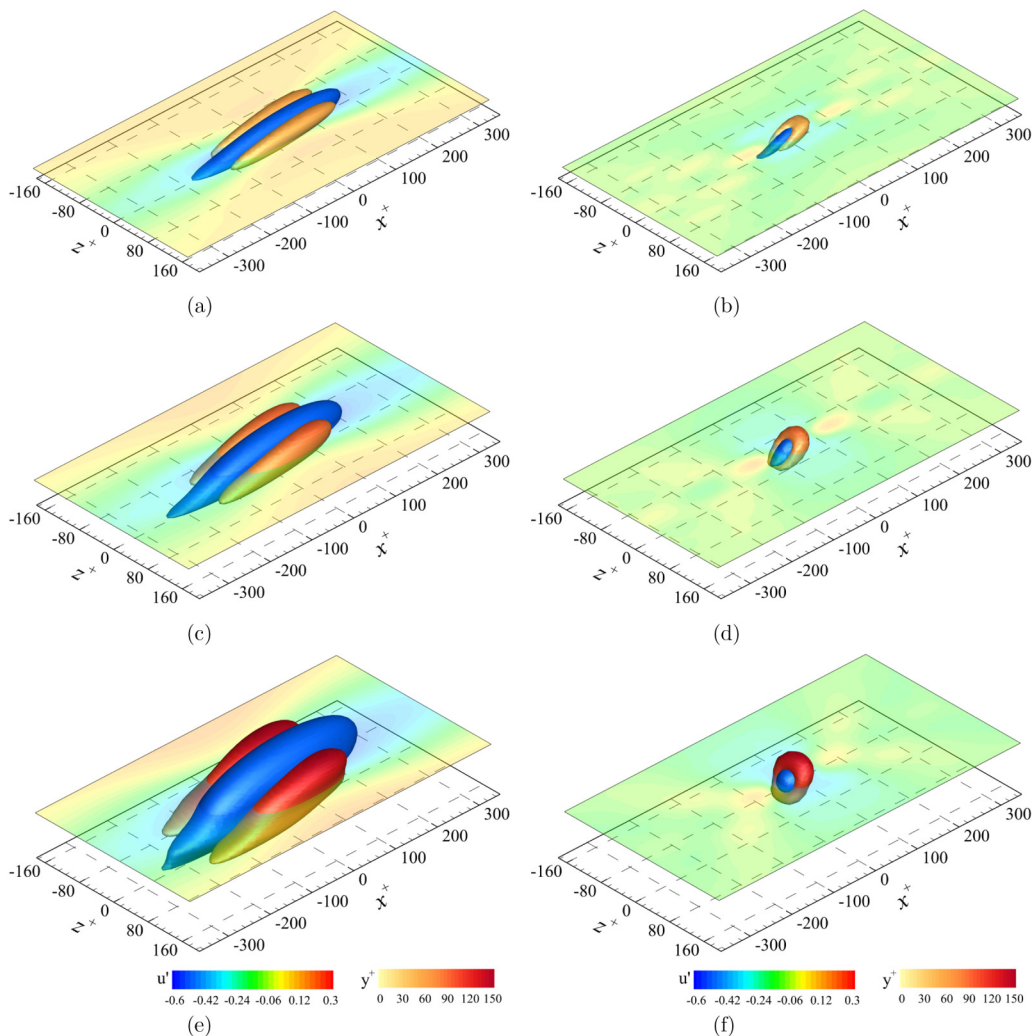


FIG. 13. Isosurfaces of conditionally averaged large-scale fields (a), (c), (e) and small-scale fields (b), (d), (f) given a low-velocity event in the original DNS data at reference location $y^+ = 30$ (a), (b), 60 (c), (d), and 100 (e), (f). The Reynolds number is 550. Condition is for $u' \leq -u'_{\text{rms}}$ at each reference location. The vortex structures are visualized using the Q vortex detection criterion with $Q = 0.2Q_{\text{max}}$ and colored based on the wall-normal height. The blue isosurface indicates the low-speed streamwise velocity region at $u' = -0.5u'_{\text{max}}$. The contour map of the streamwise velocity is plotted in the x - z plane at the reference location.

We tested different thresholds to select for the event, and there was no apparent difference between those averaged coherent structures. The averaged data are the large-scale fields and the small-scale fields.

The conditionally averaged coherent structures of the large-scale fields (a, c, e) and small-scale fields (b, d, f) are given in Fig. 13, and the reference positions y^+_{ref} for Figs. 13(a) and 13(b), Figs. 13(c) and 13(d), and Figs. 13(e) and 13(f) are 30, 60, and 100, respectively. The isosurfaces colored by wall-normal height represent the vortical structure with $Q = 0.2Q_{\text{max}}$. The blue isosurface indicates the low-speed streamwise velocity region at $u' = -0.5u'_{\text{max}}$. Figure 13(a) clearly shows the combination of the streaks and quasi-streamwise vortices associated with the near-wall circle. The streaks and quasi-streamwise vortices are almost parallel to the wall. As y^+

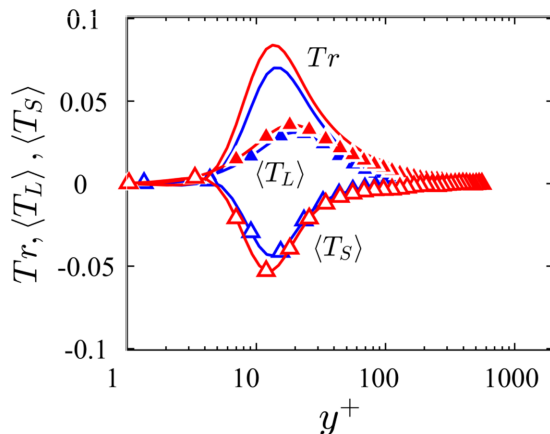


FIG. 14. Wall-normal distribution of interscale energy transfer Tr (the solid lines), $\langle T_L \rangle$ (the solid symbols), and $\langle T_S \rangle$ (the hollow symbols) at $Re_\tau = 180$ (blue) and 550 (red).

increases, the spanwise scales of the low-speed region and the vortical structure also increase, as does the inclination angle of the quasi-streamwise vortices. In the outer layer ($y^+ = 100, 0.18\delta$), the conditionally averaged flow structures of the large scales are very similar to those in the near-wall region. The low-speed zone is flanked by two quasi-streamwise vortices that are attached to the wall. Although the threshold of the isosurface is reduced to a very low value as $Q = 0.05Q_{\max}$, the heads of these two quasi-streamwise vortices will not connect with each other. This implies that the strength of the spanwise vortex is much smaller than that of the quasi-streamwise vortex in large-scale fields. However, in Figs. 13(b), 13(d) and 13(f), the conditionally averaged vortex structures of the small scales can be interpreted as the head and neck of a hairpin vortex [72,75]. In contrast to the conditional results given in Fig. 18 from Ref. [72], there is no elongated low-speed region underneath the hairpin head or between its legs. These results may indicate that large-scale motions are generated by large streamwise vortices. This conclusion is consistent with the response mode obtained using the resolvent analysis proposed in Ref. [41]. Those authors also state that energetic large-scale structures arise naturally from resolvent analysis rather than by a summation of hairpin packets [41].

We also consider the conditionally averaged flow structures corresponding to the real-space energy transfer. In this part, the superscripts $(\cdot)^L$ and $(\cdot)^S$ are used to denote the large scales and small scales, respectively. Since the velocity field is decomposed using a Fourier filter, the cross-correlation $\langle u^L u^S \rangle$ yields zero [48,61]. Reference [61] derived the transport equation for the energy of the large- and small-scale flow fields. The interscale energy transfer between these two scales can be expressed as

$$Tr = \underbrace{\left\langle -u_i^S u_j^S \frac{\partial u_i^L}{\partial x_j} \right\rangle}_{T_L} - \underbrace{\left\langle -u_i^L u_j^L \frac{\partial u_i^S}{\partial x_j} \right\rangle}_{T_S}. \quad (5)$$

According to Motoori and Goto [61], the first term T_L on the right-hand side can be used to interpret the energy transfer from the large to small scales, and the second term T_S means the energy transfer from small to large scales. We plot the wall-normal distribution of Tr , $\langle T_L \rangle$, and $\langle T_S \rangle$ in Fig. 14 by solid lines, solid symbols, and hollow symbols, respectively. Clearly, on average, T_L is always positive and T_S is always negative across the boundary layer. Therefore, the Tr is always larger than zero. This implies that the energy cascade is from large scales to small scales on average. Another feature in Fig. 14 is that the peak of T_L locates higher than that of T_S .

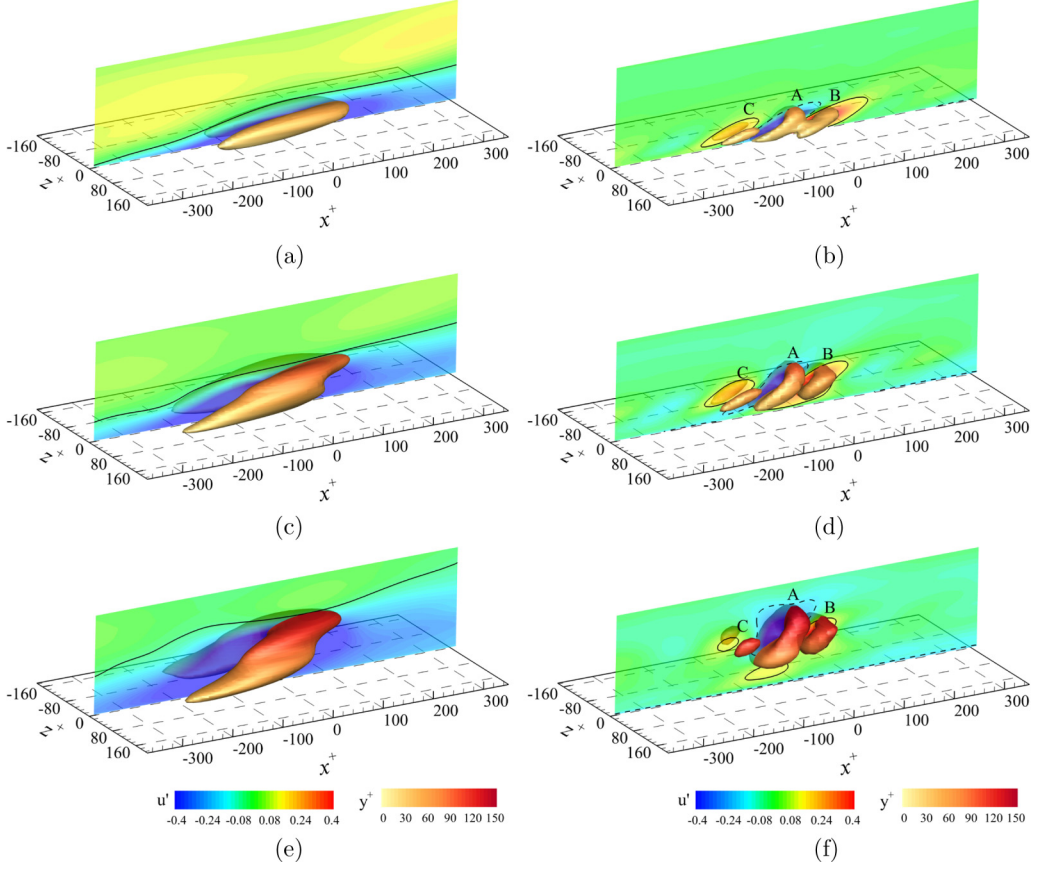


FIG. 15. Conditionally averaged coherent structures corresponding to the events $T_L \geq T_{L,rms}$ (a), (c), (e) and $T_S \leq -T_{S,rms}$ (b), (d), (f) at reference location $y^+ = 30$ (a), (b), 60 (c), (d), and 100 (e), (f) for $Re_\tau = 550$. The vortex structures are visualized using the Q vortex detection criterion with $Q = 0.2Q_{max}$ (a), (c), (e) and $Q = 0.04Q_{max}$ (b), (d), (f), and colored based on the wall-normal height. The contour map of the streamwise velocity at $z^+ = 0$ is also plotted. The solid black lines in panels (a), (c), and (e) indicate the zero-cross boundaries of the streamwise velocity, and the solid and dashed black lines in panels (b), (d), and (f) represent $u' = 0.1$ and -0.15 , respectively.

To analyze how the vortical structures are created by the forward energy cascade, conditionally averaged coherent structures corresponding to T_L and T_S are computed as shown in Fig. 15. The large-scale fields are averaged on the condition of $T_L \geq T_{L,rms}$, and the results are shown in the left plane. The small-scale fields are conditioned for the $T_S \leq -T_{S,rms}$ event, and the results are shown in the right plane. These events correspond to intense forward energy cascade. The reference position y_{ref}^+ is 30, 60, and 100 from top to bottom. The Reynolds number is 550. On the one hand, the large-scale coherent structures associated with $T_L \geq T_{L,rms}$ still consist of low-speed streaks and quasi-streamwise vortices. However, the quasi-streamwise vortices connect with each other even for higher Q threshold. This implies that an intense shear layer exists in the wall-normal direction. We also present the isocontours of $u' = 0$ as black solid lines in Figs. 15(a), 15(c) and 15(e) to clearly show the shear layer. It can be concluded that the forward energy cascade always happens at the large-scale shear layer. On the other hand, the small-scale coherent structures associated with $T_S \leq -T_{S,rms}$, as shown in Figs. 15(b), 15(d) and 15(f), present periodic distributions along the streamwise direction. All the hairpins are downstream inclined and consist of prograde hairpins (their head

rotation is in the same sense as the mean shear, indicated by A) and retrograde hairpins (their head rotation is opposite to the mean shear, indicated by B and C) in Fig. 15. There are two reasons for the existence of a retrograde hairpin. One is that a retrograde hairpin indeed exists in the wall turbulence [49,76]. Another reason is that the local mean shear velocity associated with the large scales, as shown in Figs. 15(a), 15(c) and 15(e), is subtracted. With the local mean velocity profile added, the retrograde vortices can be suppressed [41]. Back to the energy cascade, the coherent structures shown in Fig. 15 indicate that the small-scale vortices may be created by an intense large-scale shear layer, which may reveal the process of the forward energy cascade. In other words, the large scales provide a background flow to locally generate small-scale vortices.

V. DISCUSSION AND CONCLUSIONS

The flow structures corresponding to the interscale energy transfer spectra are analyzed to shed light on the relationship between hairpin vortices and large-scale flow fields. The DNS data of channel turbulent flow at $Re_\tau = 180$ and 550 are used in this paper. The relevant discussions and conclusions are summarized as follows.

(1) The flow fields are decomposed to energy-containing large scales and vortex-dominated small scales according to the interscale transfer spectra consisting of the negative region and the positive region. The negative region considerably overlaps with the peak of the energy spectra and the region of spectral production. The large-scale fields, which are dominated by energetic streamwise-elongated coherent structures, are extracted by using the negative region as a mask to filter the spectral space [20]. Bandpass filtering can be also applied to perform scale decomposition [61,77]; however, this technique cannot easily identify the real vortex-dominated small scales due to the inhomogeneity and anisotropy of wall-bounded turbulence. For the method used in the present paper, the shape of this filter varies with the wall-normal location and presents anisotropic characteristics in the streamwise and spanwise directions. Furthermore, no artificial or subjective thresholds are required in this method. One limitation is that this method needs a large dataset to obtain statistically converged interscale energy transfer spectra.

(2) As shown in Fig. 8, the large-scale fields are more suitable to be represented by the velocity, whereas the small-scale fields are more suitable to be characterized by vortices (velocity gradient). This can be used to understand the reason why velocity is used to investigate LSMs or VLSMs [61]. It is necessary to reexamine the role of hairpin vortices in fully developed turbulence as well as the relationship between the large scales and hairpin vortices [41]. Therefore, we analyzed the coherent structures associated with the real-space energy transfer, as shown in Fig. 15. The forward energy cascade is related to the large-scale shear layer and small-scale hairpin-like vortices. The large scales as a background flow field provide strong shear layers due to the existence of wall and high- and low-speed streamwise streaks, which can further induce a group of streamwise aligned hairpin-like vortices [30,40,41]. This implies that the small-scale vortices may be generated by shear instability in the outer layer rather than from the wall [61].

(3) The POD and LSE are utilized to extract the dominant coherent structures of the large scales and small scales. Both the first two POD modes and the conditionally averaged flow fields indicate that the outer large scales are formed by the elongated low-speed region and quasi-streamwise vortical structure. This coherent structure highly resembles the near-wall cycle [32–34]. Both sides of the low-speed large-scale structure are statistically flanked by quasi-streamwise vortices, as shown in Fig. 13. However, in practice, large quasi-streamwise vortices may predominantly exist on one side of the low-speed region [78]. The large vortical structures are attached to the wall, and their scales are proportional to the wall-normal height. In the present paper, the near-wall cycle and outer streak-vortex pattern are simultaneously extracted using the interscale energy transfer spectra, which indicates that the outer large-scale coherent structures may share a self-sustaining mechanism similar to that of the near-wall region. It is natural to perform DNS of minimal turbulent channels of the outer region to study the self-sustaining behavior [45,47]. In this case, the streak-vortex pattern can be isolated to show the time evolution of streaky motion. Another way to isolate

energy-containing motions is to remove smaller scales by applying explicit filtering and damp the larger scales out using the overdamped LES [42,70,79]. Hwang *et al.* [70] provided the relationship between the long streaks and the quasi-streamwise vortical structures with the self-sustaining process of the large-scale structures. Cossu and Hwang [46] even deduced that a continuum of coherent self-sustaining motions exists in the wall-bounded turbulence with scales ranging from those of buffer layer structures to those of large-scale and very-large-scale motions in the outer layer. Resolvent analysis has also been adopted to investigate the self-sustaining process of wall-bounded turbulence. Sharma and McKeon [41] suggested that the energetic streamwise structures arise naturally from resolvent analysis. Bae *et al.* [80] studied the similarities of the self-sustaining mechanism in buffer and logarithmic layers through the analysis of nonlinear mechanisms by combining resolvent analysis with numerical simulations of turbulent channel flow. In a word, a similar dynamical process may exist between the outer layer and the near-wall region.

Herein, our paper focused on the scale separation approach and the statistical flow structures for turbulent channel flows. In the future, we plan to extend this approach to a higher Reynolds number and examine the time evolution of the large-scale coherent structures and the small-scale coherent structures.

ACKNOWLEDGMENTS

This work was supported by the National Natural Science Foundation of China (NSFC) Basic Science Center Program for “Multiscale Problems in Nonlinear Mechanics” Grant No. 11988102 and by NSFC Grant No. 12072348. The authors give special thanks to W. K. Wang for helpful discussions on the interscale energy transfer spectra.

-
- [1] S. K. Robinson, Coherent motions in the turbulent boundary layer, *Annu. Rev. Fluid Mech.* **23**, 601 (1991).
 - [2] R. J. Adrian, C. D. Meinhart, and C. D. Tomkins, Vortex organization in the outer region of the turbulent boundary layer, *J. Fluid Mech.* **422**, 1 (2000).
 - [3] A. J. Smits, B. J. McKeon, and I. Marusic, High-Reynolds Number Wall Turbulence, *Annu. Rev. Fluid Mech.* **43**, 353 (2011).
 - [4] Q. Gao, C. Ortiz-Duenas, and E. K. Longmire, Analysis of vortex populations in turbulent wall-bounded flows, *J. Fluid Mech.* **678**, 87 (2011).
 - [5] J. Jiménez, Cascades in wall-bounded turbulence, *Annu. Rev. Fluid Mech.* **44**, 27 (2012).
 - [6] G. W. He, G. D. Jin, and Y. Yang, Space-time correlations and dynamic coupling in turbulent flows, *Annu. Rev. Fluid Mech.* **49**, 51 (2017).
 - [7] S. Deng, C. Pan, J. Wang, and G. He, On the spatial organization of hairpin packets in a turbulent boundary layer at low-to-moderate Reynolds number, *J. Fluid Mech.* **844**, 635 (2018).
 - [8] I. Marusic and J. P. Monty, Attached eddy model of wall turbulence, *Annu. Rev. Fluid Mech.* **51**, 49 (2019).
 - [9] A. N. Kolmogorov, The local structure of turbulence in incompressible viscous fluid for very large Reynolds numbers, *Dokl. Akad. Nauk SSSR* **30**, 301 (1941).
 - [10] S. B. Pope, *Turbulent Flows* (Cambridge University Press, Cambridge, England, 2000).
 - [11] P. Doohan, A. P. Willis, and Y. Hwang, Minimal multi-scale dynamics of near-wall turbulence, *J. Fluid Mech.* **913**, A8 (2021).
 - [12] N. Marati, C. M. Casciola, and R. Piva, Energy cascade and spatial fluxes in wall turbulence, *J. Fluid Mech.* **521**, 191 (2004).
 - [13] I. A. Bolotnov, R. T. Lahey, Jr., D. A. Drew, K. E. Jansen, and A. A. Oberai, Spectral analysis of turbulence based on the DNS of a channel flow, *Comput. Fluids* **39**, 640 (2010).
 - [14] A. Cimarelli, E. De Angelis, and C. M. Casciola, Paths of energy in turbulent channel flows, *J. Fluid Mech.* **715**, 436 (2013).

-
- [15] A. Cimarelli, E. De Angelis, P. Schlatter, G. Brethouwer, A. Talamelli, and C. M. Casciola, Sources and fluxes of scale energy in the overlap layer of wall turbulence, *J. Fluid Mech.* **771**, 407 (2015).
- [16] A. Cimarelli, E. De Angelis, J. Jiménez, and C. M. Casciola, Cascades and wall-normal fluxes in turbulent channel flows, *J. Fluid Mech.* **796**, 20 (2016).
- [17] Y. Mizuno, Spectra of energy transport in turbulent channel flows for moderate Reynolds numbers, *J. Fluid Mech.* **805**, 171 (2016).
- [18] M. Cho, Y. Hwang, and H. Choi, Scale interactions and spectral energy transfer in turbulent channel flow, *J. Fluid Mech.* **854**, 474 (2018).
- [19] A. N. Knutsen, P. Baj, J. M. Lawson, E. Bodenschatz, J. R. Dawson, and N. A. Worth, The inter-scale energy budget in a von Kármán mixing flow, *J. Fluid Mech.* **895**, A11 (2020).
- [20] W. Wang, C. Pan, and J. Wang, Energy transfer structures associated with large-scale motions in a turbulent boundary layer, *J. Fluid Mech.* **906**, A14 (2021).
- [21] F. Hamba, Inverse energy cascade and vortical structure in the near-wall region of turbulent channel flow, *Phys. Rev. Fluids* **4**, 114609 (2019).
- [22] J. L. Lumley, Spectral energy budget in wall turbulence, *Phys. Fluids* **7**, 190 (1964).
- [23] J. Jiménez, The physics of wall turbulence, *Physica A* **263**, 252 (1999).
- [24] J. A. Domaradzki, W. Liu, C. Hartel, and L. Kleiser, Energy-transfer in numerically simulated wall-bounded turbulent flows, *Phys. Fluids* **6**, 1583 (1994).
- [25] M. Lee and R. D. Moser, Spectral analysis of the budget equation in turbulent channel flows at high Reynolds number, *J. Fluid Mech.* **860**, 886 (2019).
- [26] S. Symon, S. J. Illingworth, and I. Marusic, Energy transfer in turbulent channel flows and implications for resolvent modelling, *J. Fluid Mech.* **911**, A3 (2021).
- [27] J. Jiménez, Coherent structures in wall-bounded turbulence, *J. Fluid Mech.* **842**, P1 (2018).
- [28] C. Pan, J. J. Wang, P. F. Zhang, and L. H. Feng, Coherent structures in bypass transition induced by a cylinder wake, *J. Fluid Mech.* **603**, 367 (2008).
- [29] X. H. Wu and P. Moin, Direct numerical simulation of turbulence in a nominally zero-pressure-gradient flat-plate boundary layer, *J. Fluid Mech.* **630**, 5 (2009).
- [30] J. R. Brinkerhoff and M. I. Yaras, Numerical investigation of the generation and growth of coherent flow structures in a triggered turbulent spot, *J. Fluid Mech.* **759**, 257 (2014).
- [31] Z. Zhou, G. He, and X. Yang, Wall model based on neural networks for LES of turbulent flows over periodic hills, *Phys. Rev. Fluids* **6**, 054610 (2021).
- [32] J. M. Hamilton, J. Kim, and F. Waleffe, Regeneration mechanisms of near-wall turbulence structures, *J. Fluid Mech.* **287**, 317 (1995).
- [33] J. Jiménez and A. Pinelli, The autonomous cycle of near-wall turbulence, *J. Fluid Mech.* **389**, 335 (1999).
- [34] W. Schoppa and F. Hussain, Coherent structure generation in near-wall turbulence, *J. Fluid Mech.* **453**, 57 (2002).
- [35] R. Hu and X. Zheng, Energy contributions by inner and outer motions in turbulent channel flows, *Phys. Rev. Fluids* **3**, 084607 (2018).
- [36] R. Hu, X. I. A. Yang, and X. Zheng, Wall-attached and wall-detached eddies in wall-bounded turbulent flows, *J. Fluid Mech.* **885**, A30 (2020).
- [37] I. Marusic, R. Mathis, and N. Hutchins, Predictive model for wall-bounded turbulent flow, *Science* **329**, 193 (2010).
- [38] R. Mathis, N. Hutchins, and I. Marusic, A predictive inner-outer model for streamwise turbulence statistics in wall-bounded flows, *J. Fluid Mech.* **681**, 537 (2011).
- [39] G. Yin, W.-X. Huang, and C.-X. Xu, Prediction of near-wall turbulence using minimal flow unit, *J. Fluid Mech.* **841**, 654 (2018).
- [40] X. Wu, P. Moin, J. M. Wallace, J. Skarda, A. Lozano-Durán, and J.-P. Hickey, Transitional-turbulent spots and turbulent-turbulent spots in boundary layers, *Proc. Natl. Acad. Sci. USA* **114**, E5292 (2017).
- [41] A. S. Sharma and B. J. McKeon, On coherent structure in wall turbulence, *J. Fluid Mech.* **728**, 196 (2013).
- [42] S. Rawat, C. Cossu, Y. Hwang, and F. Rincon, On the self-sustained nature of large-scale motions in turbulent Couette flow, *J. Fluid Mech.* **782**, 515 (2015).

- [43] Y. Hwang and B. Eckhardt, Attached eddy model revisited using a minimal quasi-linear approximation, *J. Fluid Mech.* **894**, A23 (2020).
- [44] F. Waleffe, On a self-sustaining process in shear flows, *Phys. Fluids* **9**, 883 (1997).
- [45] O. Flores and J. Jiménez, Hierarchy of minimal flow units in the logarithmic layer, *Phys. Fluids* **22**, 071704 (2010).
- [46] C. Cossu and Y. Hwang, Self-sustaining processes at all scales in wall-bounded turbulent shear flows, *Phil. Trans. R. Soc. A* **375**, 20160088 (2017).
- [47] A. Lozano-Duran, H. J. Bae, and M. P. Encinar, Causality of energy-containing eddies in wall turbulence, *J. Fluid Mech.* **882**, 23 (2020).
- [48] T. Kawata and P. H. Alfredsson, Inverse Interscale Transport of the Reynolds Shear Stress in Plane Couette Turbulence, *Phys. Rev. Lett.* **120**, 244501 (2018).
- [49] S. W. Dong, Y. X. Huang, X. X. Yuan, and A. Lozano-Duran, The coherent structure of the kinetic energy transfer in shear turbulence, *J. Fluid Mech.* **892**, 17 (2020).
- [50] C. Bauer, A. von Kameke, and C. Wagner, Kinetic energy budget of the largest scales in turbulent pipe flow, *Phys. Rev. Fluids* **4**, 064607 (2019).
- [51] B. Q. Deng and C. X. Xu, Influence of active control on STG-based generation of streamwise vortices in near-wall turbulence, *J. Fluid Mech.* **710**, 234 (2012).
- [52] B. Q. Deng, W. X. Huang, and C. X. Xu, Origin of effectiveness degradation in active drag reduction control of turbulent channel flow at $Re_\tau = 1000$, *J. Turbul.* **17**, 758 (2016).
- [53] See, <https://turbulence.oden.utexas.edu/>.
- [54] J. C. d. Álamo and J. Jiménez, Spectra of the very large anisotropic scales in turbulent channels, *Phys. Fluids* **15**, L41 (2003).
- [55] S. Hoyas and J. Jiménez, Reynolds number effects on the Reynolds-stress budgets in turbulent channels, *Phys. Fluids* **20**, 101511 (2008).
- [56] W. J. Baars, N. Hutchins, and I. Marusic, Spectral stochastic estimation of high-Reynolds-number wall-bounded turbulence for a refined inner-outer interaction model, *Phys. Rev. Fluids* **1**, 054406 (2016).
- [57] S. Hoyas and J. Jiménez, Scaling of the velocity fluctuations in turbulent channels up to $Re_\tau = 2003$, *Phys. Fluids* **18**, 011702 (2006).
- [58] I. Marusic, R. Mathis, and N. Hutchins, High Reynolds number effects in wall turbulence, *Int. J. Heat Fluid Flow* **31**, 418 (2010).
- [59] H. P. Wang, S. Z. Wang, and G. W. He, The spanwise spectra in wall-bounded turbulence, *Acta Mech. Sin.* **34**, 452 (2018).
- [60] H. Wang and Q. Gao, A study of inner-outer interactions in turbulent channel flows by interactive POD, *Theor. Appl. Mech. Lett.* **11**, 100222 (2021).
- [61] Y. Motoori and S. Goto, Hierarchy of coherent structures and real-space energy transfer in turbulent channel flow, *J. Fluid Mech.* **911**, A27 (2021).
- [62] B. J. Balakumar and R. J. Adrian, Large- and very-large-scale motions in channel and boundary-layer flows, *Phil. Trans. R. Soc. A* **365**, 665 (2007).
- [63] J. M. Wallace, Quadrant analysis in turbulence research: History and evolution, *Annu. Rev. Fluid Mech.* **48**, 131 (2016).
- [64] L. H. O. Hellström, I. Marusic, and A. J. Smits, Self-similarity of the large-scale motions in turbulent pipe flow, *J. Fluid Mech.* **792**, R1 (2016).
- [65] L. Sirovich, Turbulence and the dynamics of coherent structures. I: Coherent structures. II: Symmetries and transformations. III: Dynamics and scaling, *Q. Appl. Math.* **45**, 561 (1987).
- [66] A. A. Townsend, *The Structure of Turbulent Shear Flow*, Cambridge Monographs on Mechanics and Applied Mathematics (Cambridge University Press, Cambridge, England, 1976).
- [67] S. D. Muralidhar, B. Podvin, L. Mathelin, and Y. Fraigneau, Spatio-temporal proper orthogonal decomposition of turbulent channel flow, *J. Fluid Mech.* **864**, 614 (2019).
- [68] A. Towne, O. T. Schmidt, and T. Colonius, Spectral proper orthogonal decomposition and its relationship to dynamic mode decomposition and resolvent analysis, *J. Fluid Mech.* **847**, 821 (2018).

- [69] L. I. Abreu, A. V. G. Cavalieri, P. Schlatter, R. Vinuesa, and D. S. Henningson, Spectral proper orthogonal decomposition and resolvent analysis of near-wall coherent structures in turbulent pipe flows, *J. Fluid Mech.* **900**, A11 (2020).
- [70] Y. Hwang, A. P. Willis, and C. Cossu, Invariant solutions of minimal large-scale structures in turbulent channel flow for Re_τ up to 1000, *J. Fluid Mech.* **802**, R1 (2016).
- [71] R. Blackwelder, Role of phase information in conditional sampling, *Phys. Fluids* **20**, S232 (1977).
- [72] D. J. C. Dennis and T. B. Nickels, Experimental measurement of large-scale three-dimensional structures in a turbulent boundary layer. Part 1. Vortex packets, *J. Fluid Mech.* **673**, 180 (2011).
- [73] H. Nobach, C. Tropea, L. Cordier, J.-P. Bonnet, J. Delville, J. Lewalle, M. Farge, K. Schneider, and R. Adrian, Review of some fundamentals of data processing, in *Springer Handbook of Experimental Fluid Mechanics*, edited by C. Tropea, A. L. Yarin, and J. F. Foss (Springer-Verlag, Berlin, Heidelberg, 2007), pp. 1337–1398.
- [74] G. E. Elsinga, C. Poelma, A. Schröder, R. Geisler, F. Scarano, and J. Westerweel, Tracking of vortices in a turbulent boundary layer, *J. Fluid Mech.* **697**, 273 (2012).
- [75] C. Wang, Q. Gao, J. Wang, B. Wang, and C. Pan, Experimental study on dominant vortex structures in near-wall region of turbulent boundary layer based on tomographic particle image velocimetry, *J. Fluid Mech.* **874**, 426 (2019).
- [76] V. K. Natrajan, Y. Wu, and K. T. Christensen, Spatial signatures of retrograde spanwise vortices in wall turbulence, *J. Fluid Mech.* **574**, 155 (2007).
- [77] A. Lozano-Duran, M. Holzner, and J. Jiménez, Multiscale analysis of the topological invariants in the logarithmic region of turbulent channels at a friction Reynolds number of 932, *J. Fluid Mech.* **803**, 356 (2016).
- [78] K. Kevin, J. Monty, and N. Hutchins, The meandering behaviour of large-scale structures in turbulent boundary layers, *J. Fluid Mech.* **865**, R1 (2019).
- [79] Y. Hwang and C. Cossu, Self-Sustained Process at Large Scales in Turbulent Channel Flow, *Phys. Rev. Lett.* **105**, 044505 (2010).
- [80] H. J. Bae, A. Lozano-Durán, and B. J. McKeon, Nonlinear mechanism of the self-sustaining process in the buffer and logarithmic layer of wall-bounded flows, *J. Fluid Mech.* **914**, A3 (2021).